nature portfolio

https://doi.org/10.1038/s41586-026-10495-7

Supplementary information

Purcell-enhanced spin–phonon coupling with a single colour centre

In the format provided by the authors and unedited

Supplementary Information for "Purcell-enhanced spin-phonon coupling with a single color-centre"

1 Unit Cell Design and SEM Analysis

The goal of the OMC cavity design is to achieve an optical/mechanical cavity mode pair which simultaneously enables optical readout of the SiV centre's spin properties and optomechanical readout of the mechanical mode properties. This requires high values of $\{g_{so},\ g_{om},\ g_{sm}\}$ and low values of $\{\kappa_o, \kappa_m\}$. There has been a great deal of previous work on designing mode pairs which satisfy these criteria [1]. We choose the fundamental TE-like optical mode, mechanical 'breathing mode' pair, which features a near-optimal photoelastic overlap integral between the optical E_y field component with the strain ϵ_{YY} field component, which enables large optomechanical coupling. The TE-like optical mode also supports efficient spin-photon interactions and the mechanical breathing mode supports efficient spin-phonon interactions for an SiV oriented 45° relative to the beam.

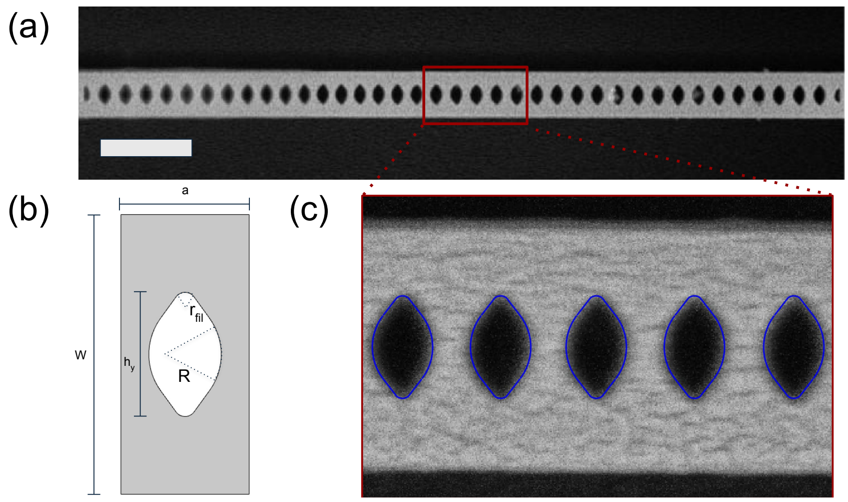

Fig. S1 (a) SEM of the cavity region of the device studied. (b) Parameterized diagram of the OMC cavity unit cell. (c) SEM of 5 unit cells in the OMC cavity with best fit unit cells drawn in blue.

The cavity region of the fabricated device is shown in Fig. S1. A unit cell design akin to the conventional elliptical hole shape is used (where the hole is defined by its major/minor axis lengths) except an additional parameter R is introduced, which determines the radius of curvature near the hole edge.

To accurately compare the experimental results to simulation, we took detailed SEM images of each unit cell hole in the OMC. Image processing on the SEM images then extracts the fabricated unit cell parameters, with the addition of the parameter r_{fil} to account for rounding at the vertical extents of the unit cell hole. For the device under study, we observe the measured parameters in Table 1.

Parameter	Measured Value	Designed Value
Beam thickness (th)	150 nm	160 nm
Beam width (w)	530 nm	540 nm
Radius (R)	110 nm	100 nm
Angle (θ)	36°	36°
Hole height (h_y)	240 nm	236 nm
Fillet radius (r_{fil})	30 nm	0 nm

Table 1 Comparison of SEM and Nominal Parameter Values

These parameters deviate from the nominal parameters of our device within normal fabrication tolerances, but do lead to measurable shifts in device properties.

2 Simulation of the Optomechanical Cavity

The optical TE-like and mechanical breathing modes were simulated using the geometric parameters obtained from SEM images (see SI section 1). Fig. S2a and Fig. S2b show the simulated profiles of these modes. The masked implantation process embeds SiV centres within a 62.5 nm x 62.5 nm area (green square shown in Fig. S2a and Fig S2b). The TE-like mode has a simulated wavelength of 736 nm and a quality factor of 3.2×10^4. The breathing mode has a simulated frequency of 12.29 GHz and a quality factor of 2.4×10^5. While the measured optical Q-factor is similar to the simulated quality factor, the measured mechanical Q-factor is much lower than the simulated value.

Finally, Fig. S2c shows the optomechanical coupling rate of the breathing mode (orange dot) as well as those of all simulated mechanical modes from 5 - 28 GHz, which covers the range of data measured as part of the spin T_1 spectrum in Fig. 4. With the exception of modes around 12 GHz, nearly all modes display negligible optomechanical coupling to the TE-like mode due to the strict symmetry requirements for such coupling [1].

3 Determination of Extrinsic Optical Cavity Loss Rate

It was observed that the quality factor and depth of resonance dip changed after the device was cleaned and cladded in ALD alumina. We suspect, but do not know, that

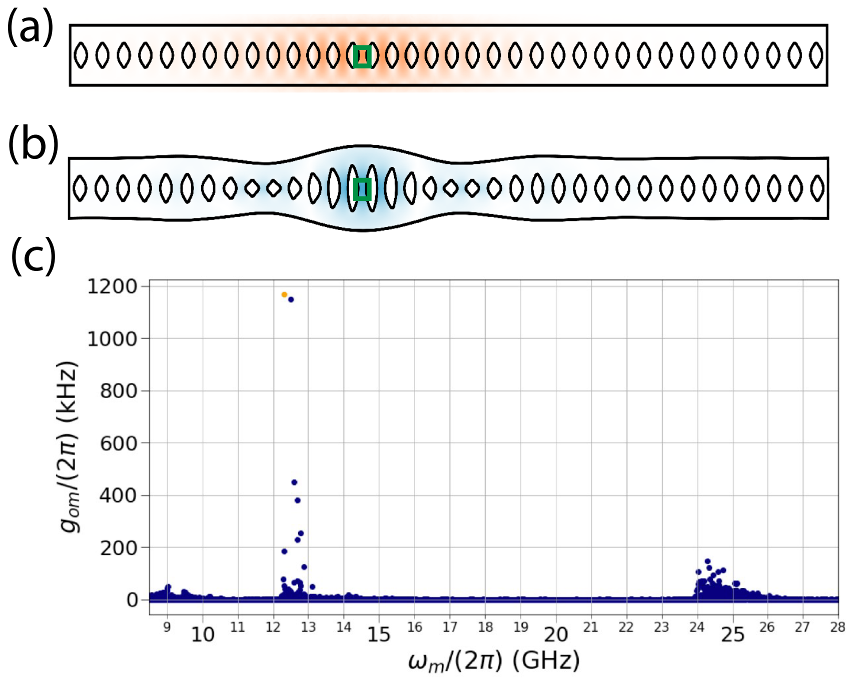

Fig. S2 (a) Electric field profile of TE-like optical mode. Green box indicates masked implantation aperture, ensuring good alignment between E-field and SiV location which enables large spin-photon coupling. (b) Strain ($\epsilon_{XX} + \epsilon_{YY} + \epsilon_{ZZ}$) profile of mechanical breathing mode. (c) Calculation of optomechanical coupling rate for full spectrum of mechanical eigenmodes. The orange dot signifies the breathing mode, showing that it satisfies the large g_{OM} requirement for optomechanical readout of the mechanical mode properties.

the cleaning was the step responsible for the slight Q_o increase. Fits to both spectra assuming an undercoupled cavity yields $\kappa_e \approx 4$ GHz. Fits assuming an overcoupled system do not yield consistent results for κ_e leading us to believe that our devices are undercoupled with $\kappa_i \approx 11$ GHz and $\kappa_e \approx 4$ GHz for the ALD alumina-cladded case. This is the best measurement of κ_e that we can make in the absence of cavity optical phase response measurements, which are difficult due to the relatively large optical linewidths of our device relative to the available bandwidth of visible-wavelength electro-optic modulators and photodetectors.

4 Power Dependent Mechanical Linewidth

With sufficiently large input power, the effects of optomechanical backaction can become significant relative to the intrinsic mechanical linewidth of the mechanical mode. Our devices are in the sideband unresolved regime where $\omega_m < \kappa$, so we use an optical probe detuning of $\Delta_o = \pm(\kappa_o/2)/(2\pi)$ to measure the blue (red) sideband

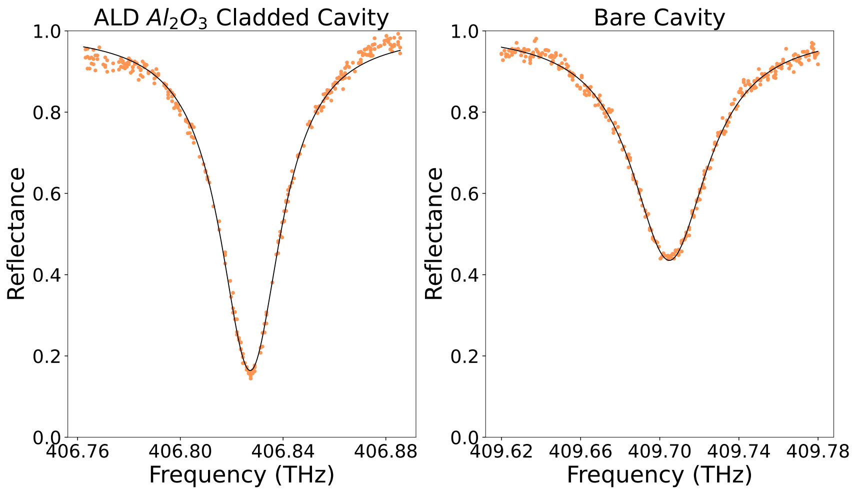

Fig. S3 Optical reflectance measurement of the bare optical cavity and the cleaned and ALD alumina cladded cavity. The total optical decay rate is ∼ 20 GHz for the bare cavity and ∼ 15 GHz for the ALD alumina clad cavity.

optical power dependence of the mechanical mode linewdith. On the blue sideband, optomechanical backaction counteracts the intrinsic damping mechanisms thereby narrowing the mechanical linewidth towards zero (the phonon lasing threshold), whereas on the red sideband, the optomechanical backaction further damps the mechanical mode. The slope of the curves in Fig. S4 are related to the optomechanical coupling rate, while the y-intercept is the intrinsic mechanical dissipation rate. The solid traces in the lower part of the plot correspond to the bare device, while the dashed traces in the upper part of the plot correspond to the same device after cladding in ALD alumina.

An increase in intrinsic linewidth from ∼350 kHz to ∼650 kHz is observed following the cladding of the OMC in alumina. Both of these values are two to three orders of magnitude narrower than the corresponding ∼12 GHz frequency feature observed in the spin decay spectrum measurement in Fig. 3. We attribute this difference to excess mechanical dissipation introduced by the gas deposition procedure required to achieve the optical resonance condition between the TE-like optical mode and the SiV centre's ZPL.

5 Calibration of Spin Transition Frequency

The spin-selective optical transition frequencies depicted in Fig. 2a shift linearly as a function of the magnitude of the applied magnetic field. Specifically, both $f_{\downarrow\uparrow'} - f_{\uparrow\uparrow'}$ and $f_{\downarrow\downarrow'} - f_{\uparrow\downarrow'}$ allow us to estimate $\omega_s/(2\pi)$. Here $f_{\uparrow\uparrow'}$ and $f_{\downarrow\downarrow'}$ are as shown in Fig. 1c. $f_{\downarrow\uparrow'}$ is the optical transition between the $|\downarrow\rangle$ and the $|\uparrow'\rangle$ state (the leftmost line in Fig. 3a) and $f_{\uparrow\downarrow'}$ is the optical transition between the $|\uparrow\rangle$ and the $|\downarrow'\rangle$ state (the

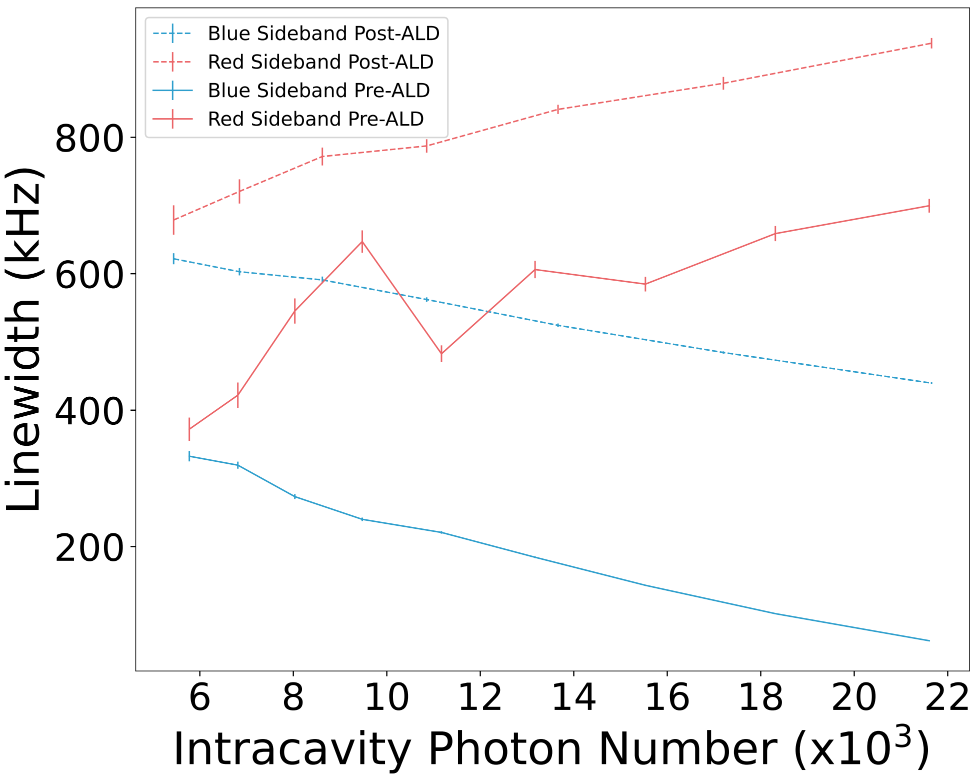

Fig. S4 Power dependent mechanical mode linewidth with laser parked on the red (blue) sideband for the red (blue) trace before (after) ALD alumina cladding is show with the solid (dashed) lines. Extrapolated intersection of the red/blue sideband curves yield an intrinsic mechanical linewidth of ~ 350 kHz (~ 650 kHz) before (after) ALD alumina cladding.

rightmost line in Fig. 3a). The optical transitions have a maximum Purcell enhanced linewidth of 3.5 GHz, which practically eliminates the effects of spectral diffusion on our experiment. For any given magnetic field orientation, a linear fit to the estimated spin transition frequency at several calibration field magnitudes yields a conversion constant between applied field magnitude and spin transition frequency. In the case of a perpendicular field shown in Fig. S5, we get a conversion constant of 2.700 ± 0.001 GHz/kG. We note that using the difference in peak frequencies of these broad optical lines is not a direct measurement of the narrow spin transition frequency. While the statistical uncertainty in this estimator is very small, reflecting its high precision, this does not account for systematic errors like differential AC stark shifts between the various optical line measurements which limit its accuracy. Here, we use these calibrations as a coarse spin-transition frequency measurement and then use sharp identifiable features in the observed spectra to line up and compare measurements under different

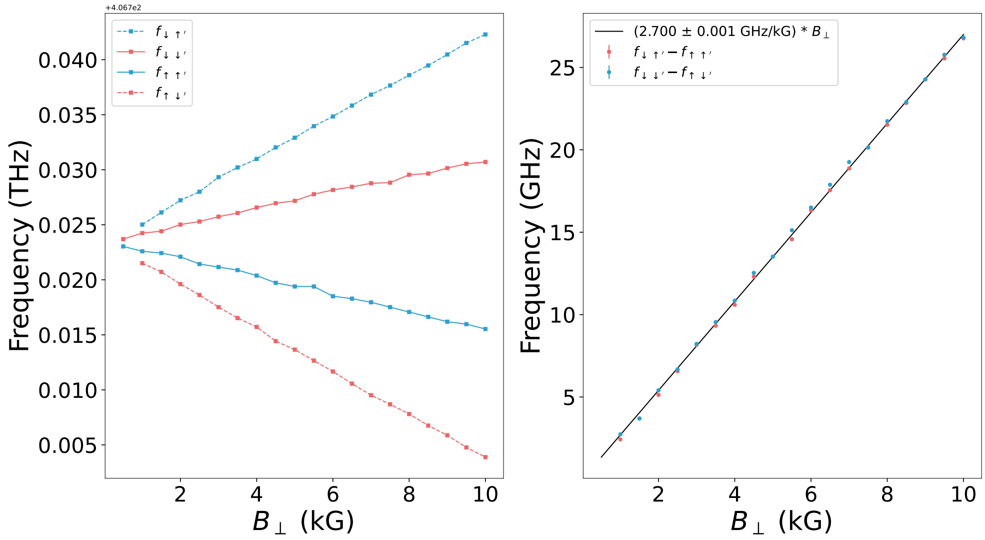

Fig. S5 Calibration of the spin transition frequency versus applied magnetic field. (a) For any given magnetic field orientation, (in this case perpendicular to the SiV centre's symmetry axis), the spin-selective optical transitions shift linearly as a function of the applied field magnitude. (b) The spin transition frequency can be estimated from $f_{\downarrow\uparrow'} - f_{\uparrow\uparrow'}$ and from $f_{\downarrow\downarrow'} - f_{\uparrow\downarrow'}$. A linear fit with zero y-intercept to these estimates yields a conversion factor between the magnetic field magnitude and the spin transition frequency (in this case, 2.7 GHz/kG).

conditions. Observation of the ~12 GHz mode (whose frequency is known to high precision from optomechanical measurements) then offers a useful reference to identify the frequency of other features with high confidence.

For our spin decay spectroscopy measurements, we use the $f_{\uparrow\uparrow'}$ and $f_{\downarrow\downarrow'}$ transitions because of their large photon scattering rate and comparatively small movement as a function of the applied magnetic field magnitude. The value of the conversion constant depends on the angle of the applied magnetic field and is calibrated at every angle for the angle-dependent measurements in Fig. 4. In particular, for a given field magnitude, a magnetic field oriented perpendicular to the SiV centre's symmetry axis will produce the minimum spin transition frequency, whereas a field aligned with the symmetry axis will produce the maximum spin transition frequency. The value of the conversion constant also depends on the static crystal strain experienced by the SiV centre, which can be inferred from the ground state orbital splitting [2]. It was observed to change after ALD alumina cladding (see SI section 9), and to a lesser extent after repeated gas tuning. Therefore, this calibration curve is retaken after any material deposition performed to tune the optical resonance.

6 Raw Data for Spin Relaxation Measurements

An example histogram of the photon counts measured by the APD connected to the time-tagger for a particular time delay τ of the optical pulse sequence is shown in Fig.

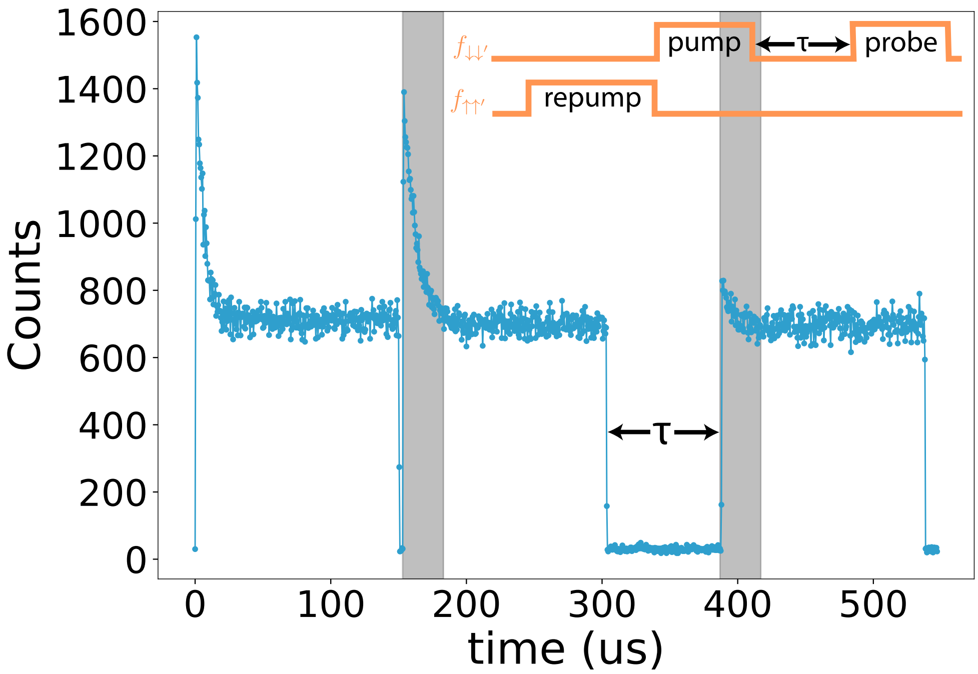

Fig. S6 An example histogram of photon detection times collected from the inset optical pulse sequence and a particular value of τ.

S6. The initialization peak seen at the beginning of each pulse corresponds to a short time of increased reflection from the device as the spin is pumped to the opposite state (shaded). The repump pulse at the beginning of the sequence, which is resonant with the $f_{\uparrow\uparrow'}$ transition, is intended to ensure that the spin population begins predominantly in the $|\downarrow\rangle$ state. Following this repump pulse, the pump and probe pulses are resonant with the $f_{\downarrow\downarrow'}$ transition. The pump pulse then pumps the spin population into the $|\uparrow\rangle$ state and produces an initial peak fluorescence corresponding to maximum population in the $|\uparrow\rangle$ state. After the variable wait time τ, the height of the initial fluorescence signal on the probe pulse relative to the height of the initialization peak on the pump pulse is a measurement of the fraction of the population that has relaxed into the $|\downarrow\rangle$ state. As τ is increased beyond the characteristic spin T_1 time, the SiV centre's spin population decays towards its thermal equilibrium value. The $f_{\uparrow\uparrow'}$ and $f_{\downarrow\downarrow'}$ transitions are nominally spin-conserving, but in a magnetic field not aligned with the SiV centre symmetry axis, this spin selection rule is relaxed and the transitions can be used to polarize the spin. In some of our spin relaxation measurements, we found that the repump pulse does not completely polarize the spin population with the maximum fidelity, however the timescale of the spin relaxation, which is the quantity of interest in our measurements, is unaffected.

7 Temperature-Dependent Spin Decay

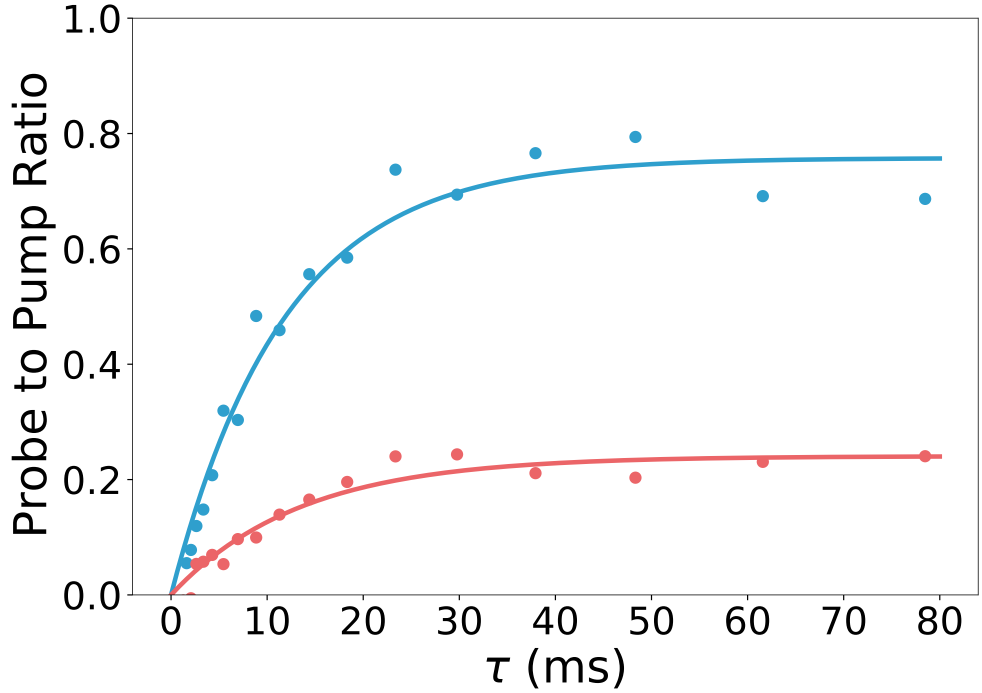

Fig. S7 Example spin decay curves measured with a 1 kG magnetic field with $\theta \approx 55°$ (corresponding to a spin transition frequency of 2.8 GHz). Blue (red) curves measured with the pump/probe laser parked on the $f_{\uparrow\uparrow'}$ ($f_{\downarrow\downarrow'}$) transition.

We performed thermometry measurements by probing the SiV centre spin relaxation with low input laser powers on the order of 1 pW. The measurement in Fig. S7 shows that intialization in the spin up state (blue data in Fig. S7) produces a greater contrast in the spin relaxation curve at long time delays (relative to $1/\gamma_s$) when compared with initialization in the spin down state (red data in Fig. S7). The data is taken at a magnetic field magnitude of 1 kG and orientation of $\theta \approx 55°$. The characteristic exponential timescale of spin relaxation for both cases is similar. At long time delays, the spin will relax to a thermal state. Based on the temperature of the SiV's environment, T and the energy difference between the spin qubit levels, $\hbar\omega_s$ the steady-state population in the spin up and down states is given by the relations:

$$p_\uparrow(\tau \gg T_1) = \frac{1}{e^{\frac{\hbar\omega_s}{k_B T}} + 1} \tag{1}$$

$$p_\downarrow(\tau \gg T_1) = 1 - \frac{1}{e^{\frac{\hbar\omega_s}{k_B T}} + 1} \tag{2}$$

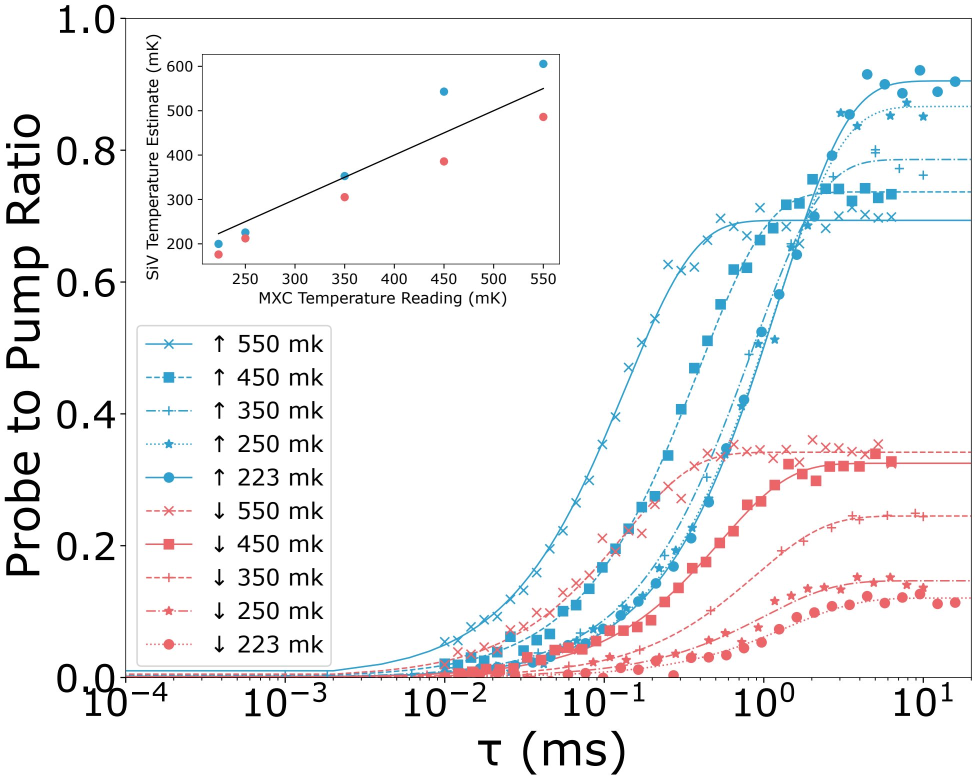

Fig. S8 Temperature dependent spin decay curves. With an applied magnetic field of 3 kG aligned with the laboratory z-axis (corresponding to a spin transition frequency of 8.3 GHz), the spin decay is measured at five different elevated temperatures. Measurements are performed on both probe transitions while applying controlled heat to the mixing plate and keeping the optical probe powers constant. Using the steady state population, an SiV temperature estimate was extracted. The inset shows a plot of this estimated SiV temperature against the temperature recorded on the MXC thermometer of the dilution fridge.

Our measurements yield an estimated SiV temperature of ~ 150 mK in the steady state. This is elevated above the thermometer readings on the copper sample mount (65 mK) and the mixing plate thermometer (44 mK), likely due to residual optical probe heating [3]. Nonetheless, at this temperature of ~ 150 mK, the 12 GHz mechanical breathing mode of our device is expected to be close to the ground state with an expected thermal phonon occupancy of 0.02 quanta. This temperature is also significantly below the temperature for $> 99\%$ population in the lower orbital branch of the SiV ground state, calculated to be $\sim$885 mK, given $\Delta_{gs} = 85$ GHz (see SI section 9). Around this temperature, the phonon population resonant with the 85 GHz ground state orbital transition can act as an additional channel for spin relaxation via an Orbach process which can dominate the direct spin-relaxation pathway [2, 4].

Fig. S8 shows the temperature-dependent spin relaxation data measured by applying a controlled amount of heat to the mixing plate of the dilution fridge. As the mixing plate temperature is raised, the spin qubit is found to decay faster with a steady state ($\tau \gg 1/\gamma_s$) population value tending towards 0.5 which corresponds to a completely mixed spin state. This behavior is expected at higher temperatures relative to the spin transition frequency. The SiV temperature estimate for each measurement can be extracted from the long-time population saturation value and is shown inset to Fig. S8. In the temperature range probed in these measurements, the SiV temperature estimate from this method is in good agreement with the temperature reading on the mixing plate thermometer.

8 Simulation of Spin-Phonon Coupling to the Mechanical Breathing Mode

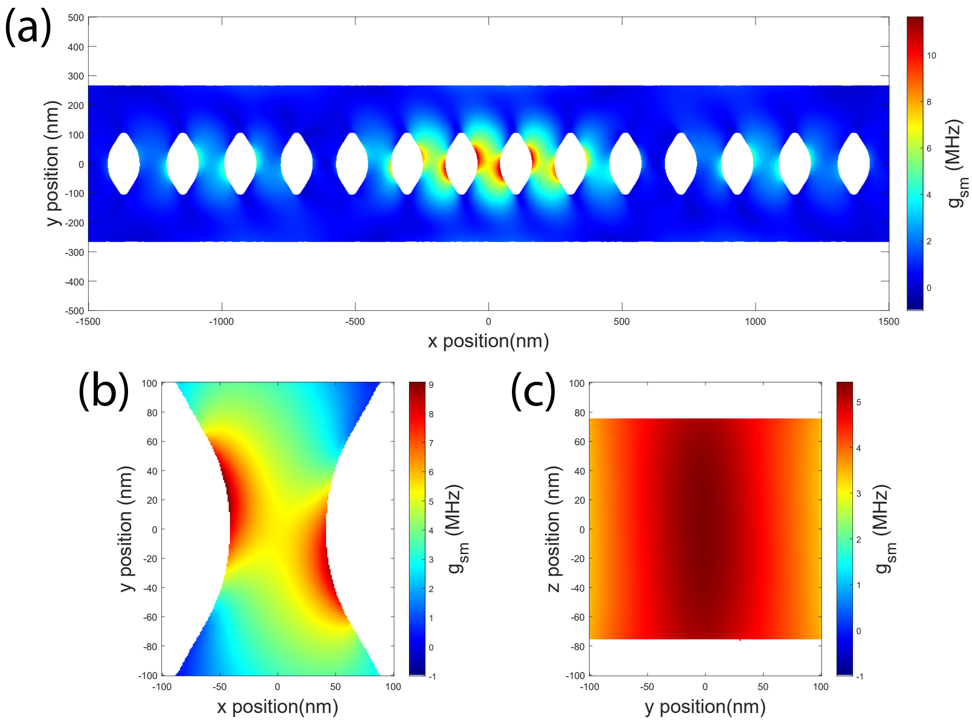

Fig. S9 (a) XY slice plot of simulated g_{sm} in the cavity region. Large g_{sm} can be realized where strain is concentrated near the cavity centre.(b) XY slice plot of simulated g_{sm} for the implantation aperture region. g_{sm} is sensitive to the in-plane location, with maximal g_{sm} found at the hole edges where strain is maximized. (c) YZ slice plot of simulated g_{sm} for the aperture region. The SiV centres are nominally implanted at the beam centre (z=0), but g_{sm} is insensitive to depth.

The strain profile of the breathing mode is used to calculate the strength of the spin-phonon coupling g_{sm} for an ideal zero static-strain SiV. Using perturbation theory [2, 5] the vacuum spin-phonon coupling rate g_{sm} is given by:

$$g_{sm} = \frac{2\gamma_s B_x}{\lambda_{SO,GS}}\sqrt{\beta^2 + \gamma^2} \tag{3}$$

where

$$\beta = d(\epsilon_{XX} - \epsilon_{YY}) + f\epsilon_{XZ} \tag{4}$$
$$\gamma = -2d\epsilon_{XY} + f\epsilon_{YZ} \tag{5}$$

and the components of the static strain tensor ϵ are in the coordinate frame of the SiV centre.

With the exception of Fig. 4b, Extended Data Fig. 3, Extended Data Fig. 4, and Extended Data Fig. 5, the data shown in this paper was taken using a magnetic field aligned to the z- axis in laboratory frame ($\theta \approx 55°$). In this case, the magnetic field component perpendicular to the SiV centre's high-symmetry axis B_X is related to the spin transition frequency by ω_s by equation $\gamma_s B_X \approx \frac{\omega_s}{\sqrt{2}}$, on resonance $\omega_s = \omega_m$. The spin-mechanical coupling rate can then be expressed as:

$$g_{sm} \approx \frac{\sqrt{2}\omega_m}{\lambda_{SO}}\sqrt{(d(\epsilon_{XX} - \epsilon_{YY}) + f\epsilon_{YZ})^2 + (-2d\epsilon_{XY} + f\epsilon_{XZ})^2} \tag{6}$$

The SiV centre's spin transition is sensitive to the strain transverse to its symmetry axis, precisely at the SiV centre's location in the cavity. Large g_{sm} can be achieved in areas of maximal strain as seen in Fig. S9 for the mechanical breathing mode of our OMC devices. Fig. S9c shows that g_{sm} is largely insensitive to depth, but highly sensitive to in-plane location. Simulations suggest that under ideal conditions of low crystal strain (strain $\ll \lambda_{so} = 46$ GHz in the orbital ground state) and a magnetic field orientation perpendicular to the high-symmetry axis of the SiV [2], g_{sm} can reach a maximum value of 9 MHz. This is roughly a factor of 30 larger than the experimentally observed g_{sm}. This difference is well explained by the non-ideal conditions in our OMC devices, in particular the non-zero static crystal strain (see SI section 9) and expected error in the SiV centre's position with respect to the strain coupling maximum.

9 Measurement of SiV Static Strain Environment

Using the gas tuning capabilities of our experiment, it is possible to tune the optical resonance of the TE-like optical mode of our devices into resonance with each of the lines in the fine structure of an optically coupled SiV centre's ZPL [6]. These measurements are performed at zero magnetic field. At ∼4K, a distinct narrow resonance within the optical reflection spectrum is observed at the frequency resonant with the atomic line [7, 8]. Knowledge of the frequency splittings of an SiV centre's fine structure is useful because it can be used as a measurement of the static crystal strain experienced by the SiV centre. The data in Fig. S10 was taken after the device was

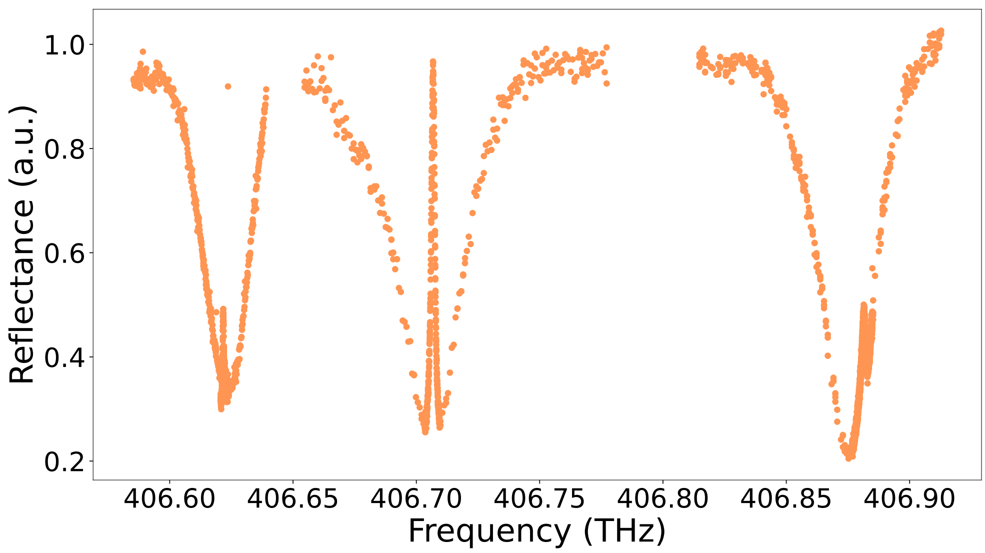

Fig. S10 Optical reflection spectrum of the SiV cavity system with the optical cavity (broader feature) gas tuned into resonance with the D (left), C (middle), and B (right) optical transitions in the SiV fine structure. From the measured optical transition frequencies we infer a ground state splitting $\Delta_{gs} = 85$ GHz and an excited state splitting $\Delta_{es} = 260$ GHz corresponding to a moderately strained SiV center.

clad in ALD alumina making it impossible to reach the bluest transition (the A-line). However, the observation of three lines is sufficient to measure the ground and excited state splittings ($\Delta_{gs} = 85$ GHz and $\Delta_{es} = 260$ GHz respectively). Note that at millikelvin temperatures where the ground state phonon transition is frozen out, the B and D line go dark due to a lack of population in the upper branch of the ground state, making them unsuitable for measurements in this temperature range.

10 Simulation of Spin-Phonon Coupling to the Broadband Acoustic Density of States

While our design work focused on the mechanical breathing mode, the coupling of the SiV centre to mechanical modes in the 8.5-28 GHz frequency range was measured and simulated as seen in Fig. S11. To model the phonon-induced decay of the SiV centre as a function of the spin transition frequency, we sum the contributions from all of these modes:

$$\Gamma(\omega) = 4 \sum_q \frac{g_q^2 \kappa_q}{\kappa_q^2 + 4(\omega_q - \omega)^2} \tag{7}$$

To account for the fact that the experimentally observed quality factor ($Q_q = \frac{\omega_q}{\kappa_q}$) is lower than what is simulated, we include a phenomenological reduction in Q so that $Q'_q = (Q_{sim}^{-1} + Q_{damp}^{-1})^{-1}$, where $Q_{damp} = 350$ based on the experimentally observed linewidth broadening of the breathing mode. We also account for the static-strain of the SiV as measured in section 9, which leads to a reduction in g_q.

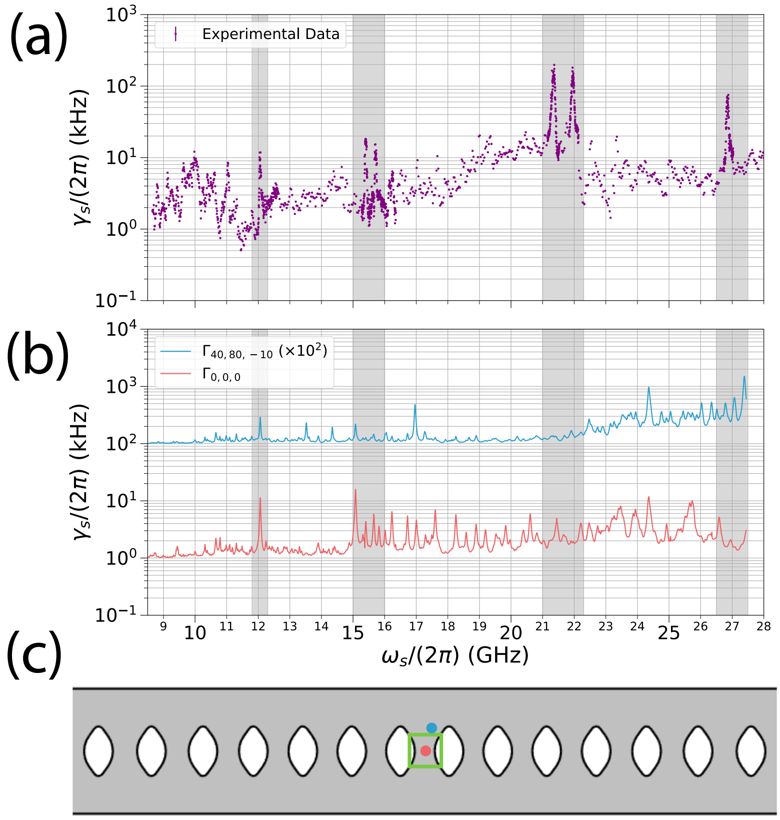

Fig. S11 (a) Broadband spin decay spectrum for a $\theta \approx 55°$ magnetic field, also shown in Fig. 4. Shaded regions indicate observed resonances of increased Purcell enhancement, attributed to localized mechanical modes. (b) Simulated spin decay spectrum $\Gamma_{x,y,z}$ for different choices of SiV-centre location relative to the cavity centre (in nm). Note that some experimental features are reproduced (namely Purcell enhancement due to the $\sim$ 12 GHz breathing mode) for both locations, but qualitatively distinct features are observed at other frequencies. (c) Cavity diagram indicating the chosen points for simulation, the implantation aperture is shown in green.

The highly local nature of spin-phonon coupling poses a modeling challenge due to the uncertain position of the SiV centre within the implantation aperture, which is 50 nm wide in both the x and y directions. As seen in Fig. S11, even a few nanometer change of the in-plane location of the SiV centre results in qualitatively distinct spin decay spectra. While this sensitivity could, in principle, be used to determine the precise SiV location, in practice, the complexity of the spectrum and the difficulty of modeling real-world imperfections—such as the aforementioned Q-factor degradation from ALD alumina and deposited gas (as shown in Fig. 3b and Extended Data Fig. 3) and device roughness and non-uniformity resulting from the quasi-isotropic etching method, limit the accuracy of such simulations. Nonetheless, many of the experimentally observed features are seen in our simulations. In particular, a resonance in the spin decay rate due to the 12 GHz breathing mode of the device can be observed consistently. The agreement of these simulations with both the spin-decay spectroscopy and optomechanical spectroscopy measurements on the 12 GHz breathing mode support the validity of this simulation approach.

Supplementary Information References

1. Chan, J., Safavi-Naeini, A. H., Hill, J. T., Meenehan, S. & Painter, O. Optimized optomechanical crystal cavity with acoustic radiation shield. *Applied Physics Letters* **101,** 081115. ISSN: 0003-6951. https://doi.org/10.1063/1.4747726 (2025) (Aug. 2012).
2. Meesala, S. *et al.* Strain engineering of the silicon-vacancy center in diamond. *Physical Review B* **97.** Publisher: American Physical Society, 205444. https://link.aps.org/doi/10.1103/PhysRevB.97.205444 (2025) (May 2018).
3. Knall, E. *et al.* Efficient Source of Shaped Single Photons Based on an Integrated Diamond Nanophotonic System. *Physical Review Letters* **129.** Publisher: American Physical Society, 053603. https://link.aps.org/doi/10.1103/PhysRevLett.129.053603 (2025) (July 2022).
4. Orbach, R. : & Bleaney, B. Spin-lattice relaxation in rare-earth salts. *Proceedings of the Royal Society of London. Series A. Mathematical and Physical Sciences* **264.** Publisher: Royal Society, 458–484. https://royalsocietypublishing.org/doi/abs/10.1098/rspa.1961.0211 (2025) (Jan. 1997).
5. Chia, C. *Quantum Optomechanics with Color Centers in Diamond* Doctoral dissertation. PhD thesis (Harvard University Graduate School of Arts and Sciences, Cambridge, MA, May 2021). https://nrs.harvard.edu/URN-3:HUL.INSTREPOS:37368314.
6. Hepp, C. *et al.* Electronic Structure of the Silicon Vacancy Color Center in Diamond. *Physical Review Letters* **112.** Publisher: American Physical Society, 036405. https://link.aps.org/doi/10.1103/PhysRevLett.112.036405 (2025) (Jan. 2014).
7. Waks, E. & Vuckovic, J. Dipole Induced Transparency in Drop-Filter Cavity-Waveguide Systems. *Physical Review Letters* **96.** Publisher: American Physical Society, 153601. https://link.aps.org/doi/10.1103/PhysRevLett.96.153601 (2025) (Apr. 2006).
8. Sipahigil, A. *et al.* An integrated diamond nanophotonics platform for quantum-optical networks. *Science* **354.** Publisher: American Association for the Advancement of Science, 847–850. https://www.science.org/doi/full/10.1126/science.aah6875 (2025) (Nov. 2016).